Interface-driven superconductivity in FeSe/SrTiO$_3$ from first-principles

R. Reho[1*], N. Wittemeier[2†] and A. H. Kole[1] A. R. Botello-Méndez[1] Z. Zanolli[1]

1 Chemistry Department and Debye Institute for Nanomaterials Science, Condensed Matter and Interfaces, Utrecht University and ETSF, PO Box 80.000, 3508 TA Utrecht, The Netherlands
2 Catalan Institute of Nanoscience and Nanotechnology (ICN2) and European Theoretical Spectroscopy Facility, CSIC, BIST, Campus UAB, Bellaterra, 08193 Barcelona, Spain

⋆ r.reho@uu.nl ,   † nils.wittemeier@icn2.cat

Abstract

We investigate the superconducting properties of monolayer FeSe, both freestanding (ML FeSe) and on SrTiO$_3$ (STO), by simultaneously solving the Kohn-Sham Density Functional Theory and Bogoliubov–de Gennes equations. Our results demonstrate that the substrate profoundly alters both the normal-state and superconducting properties of FeSe. We identify proximity-induced superconductivity in the interfacial TiO$_2$ layer of STO, due to hybridization between Fe d and O p orbitals. This hybridization results in a fivefold increase in the superconducting gap width and confines superconducting states to the M point in the Brillouin Zone. This is in contrast to ML FeSe, where superconductivity emerges at both the Γ and M points. Furthermore, the substrate modifies the orbital character of the states responsible for superconductivity, which change from Fe d_{z^2} in ML FeSe to Fe d_{xz}/d_{yz} in FeSe/STO. In both systems, we demonstrate an anisotropic superconducting gap with multiple coherence peaks, originating at different k-points in the Brillouin Zone. Additionally, in FeSe/STO, we identify emerging states unique to the superconducting phase arising from electron-hole hybridization at M, in agreement with experiments. Our findings highlight the decisive impact of substrate (hybridization, strain, charge transfer, magnetic order) on the superconducting properties of FeSe. We suggest potential pathways for engineering novel high-temperature FeSe-based superconductors by leveraging interfacial interactions in substrates with high electron affinity.

1 Introduction

Monolayer (ML) FeSe on SrTiO$_3$ (FeSe/STO) features high critical temperature (T$_C$∼ 40–100 K) making it appealing for both fundamental research and development of next-generation quantum devices [1–3]. The electronic dispersion of FeSe is highly sensitive to factors such as magnetic configurations, structural changes (strain) and the dielectric environment (doping and dipole interactions) [4]. The presence of a substrate affects all the above properties which, in turn, directly influence the superconducting pairing mechanism [5]. Experiments

on FeSe/STO proved the conventional BCS–like s–wave nature of the superconducting pairing potential [6]. *Zhang et al.* [7] reported two anisotropic superconducting gaps driven by Fe d_{xz}/d_{yz} (20 meV wide) and Fe d_{xy} (26 meV wide), reflecting the multiorbital nature of the Fermi surface and the orbital–dependent pairing in iron chalcogenides. Currently, it is still unclear whether FeSe/STO exhibits single or double coherence peaks [8], the interplay between its magnetic and electronic properties is not fully understood, the agreement between theoretical predictions and experiments is incomplete, and the origin of high T_C is unknown.

Tight-binding models of FeSe ML and FeSe/STO successfully describe specific experiments but lack general applicability [1, 8] and are restricted to a normal state description. State-of-the-art theoretical studies [9–11] combine dynamical mean field theory (DMFT) and the quasiparticle self-consistent GW approximation to describe the superconducting instability of FeSe/STO from the spin and charge response of the system. These studies explain the dependence of the critical temperature on doping and Fe-O interaction. This method includes electron correlations and requires careful parameter tuning.

In this work, we simultaneously solve the Kohn-Sham Density Functional Theory (DFT) and Bogoliubov–de Gennes (BdG) equations [12, 13] to analyze and interpret both the normal and superconducting states of ML FeSe and FeSe/STO. Our findings highlight the significant impact of the substrate on the superconducting (SC) phase of FeSe, and emphasize how interface-driven superconductivity can be leveraged to enhance superconductivity in FeSe. In the normal state, metallicity in ML FeSe arises from an electron pocket a M and a hole pocket along the $\Gamma - X$. In contrast, in FeSe/STO, the hole pocket shifts to lower energies within the valence band. This difference influences the mechanism behind superconductivity. In the superconducting phase, we predict proximity-induced superconductivity on the interfacial O atoms and a fivefold widening of the SC gap in FeSe/STO compared to ML FeSe. We elucidate the origins of superconducting coherence peaks in the superconducting density of states (SC–DOS) of both system, identifying univocally the real-space orbitals and momentum vector **k** associated with these peaks. We characterize the Bogoliubov–de Gennes spectrum and predict an anisotropic, momentum-dependent superconducting gap $\Delta(\mathbf{k})$ for both system. We analyze the changes in electronic dispersion between freestanding ML FeSe and FeSe/STO, identifying the dominant roles of Fe d and O p orbitals in shaping the Fermi surface. We conclude that FeSe and FeSe/STO act as fundamentally different materials, as substrate hybridization, interfacial interactions and charge transfer play a crucial role in shaping the microscopic superconducting mechanism. This behaviour can be generalized to the whole family of iron pnictides. Substrate engineering presents a promising approach to design superconductors with enhanced T_C.

2 Structural properties

In the following, we focus on the tetragonal phase of ML FeSe, in view of comparing it with Fe/STO [1]. The primitive unit cell of FeSe consists of two Fe and two Se atoms. The Fe atoms form two tetragonal sub–lattices, offset relative to each other [Fig. 1.(a)]. The Se atoms form tetrahedra centered on the Fe atoms. After structural relaxation, the lattice parameter of ML FeSe is 3.71 Å and the Se-Se distance is 1.44 Å. FeSe is usually grown by molecular beam epitaxy (MBE) on the TiO_2 terminated surface of STO [8]. For this reason, we first modeled STO as a six–layer slab and performed a full relaxation (atoms and unit cell), obtaining a lattice constant of 3.92 Å. The atomic positions of the FeSe/STO heterostructure were then relaxed while keeping the STO lattice fixed, resulting in 5.7% strain on FeSe ML. The FeSe/STO heterostructure was constructed by placing the bottom Se atom of FeSe directly above the top

---

[1]While single crystal FeSe undergoes a tetragonal-to-orthorhombic phase transition below 90K [5], we expect that the symmetry of the STO surface (D_4) will stabilize the tetragonal FeSe phase of FeSe in FeSe/STO [5]

53 Ti atom of the STO substrate. After relaxation, the Se-Ti distance was 2.95 Å [Fig. 3.(a)].

2.1 Magnetic instabilities

55 FeSe, both in its bulk and ML forms, exhibits a complex energy landscape characterized by
56 multiple competing magnetic configurations. The lowest-energy magnetic state of bulk FeSe
57 is theoretically predicted to be the staggered dimer phase [14]. However, long–range mag-
58 netic order is not observed in experiments [15, 16]. Indeed, bulk FeSe is a nematic quantum–
59 disordered paramagnet, interpolating between the checkerboard antiferromagnetic (CB-AFM)
60 and stripe AFM phases, both in the low (T = 4 K) and high temperature (T = 110 K) regimes [17].
61 For bulk and ML FeSe, we computed first-principles total energies of various magnetic config-
62 urations (Appendix A). In both cases, we found three low-energy competing magnetic con-
63 figurations: staggered trimer, staggered dimer, and single stripe, followed by two CB-AFM
64 phases (in- and out-of-plane) with similar total energies, approximately 68 meV above the
65 lowest-energy configurations. We find that only the band structure of the out-of-plane CB
66 phase [Fig. 1.(a)] resembles the ARPES electronic dispersion [4,18]. For this reason, we focus
67 on the CB phase despite its higher total energy compared to the other phases.

2.2 Normal state electronic properties

69 The normal state band structure of ML FeSe features an electron pocket at M, a hole pocket
70 along the $\Gamma - X$ high-symmetry line, and a relative maximum in the highest occupied valence
71 band along the $\Gamma - M$ line [Fig. 1.(b)]. Analysis of the Mulliken populations [19] reveals that
72 FeSe acquires 0.13 electrons (per unit cell) from STO in the FeSe/STO heterostructure. As a
73 result, the hole pocket along the $\Gamma - X$ direction is pushed below the Fermi-level, and the top
74 valence band becomes flatter [Fig. 3.(b)].

75 The origin of metallicity in FeSe changes due to the interaction with the substrate: in
76 the freestanding ML, metallicity is associated with the electron and a hole pocket, while in
77 FeSe/STO only to the electron pocket at M. Analysis of the Fermi surfaces (Fig. 16) facilitate
78 the visualization of these concepts: In FeSe ML, the hole pocket along $\Gamma - X$ is clearly visible
79 in Fig. 16.(a), while the relative maxima along $\Gamma - M$ lies tens of meV lower in energy. In
80 FeSe/STO, instead, the hole pocket near Γ disappears. At M, the electron pocket of FeSe/STO
81 has a more pronounced hyperbolic shape with respect to FeSe ML [Fig. 16.(b)]. This will have
82 consequences in the superconducting behaviour of the two materials.

83 Orbital projected band structures of FeSe and FeSe/STO [Fig. 2] show that the orbitals as-
84 sociated to the electron pocket at M are Fe d_{xz}, d_{yz}, and, to a lesser extent, d_{xy}. In FeSe/STO
85 [Fig. 15] a hole pocket associated to interfacial O p_x/p_y states emerges at M. In the supercon-
86 ducting phase of FeSe/STO, the Fe d states hybridize with O p_x and O p_y and are responsible
87 for the opening of the superconducting gaps at M, as predicted by *Acharya* et al. [9–11].

2.3 Superconducting state

89 In order to model the superconducting phase, we solve the SIESTA–BdG equations using the
90 *fixed–Δ* approach [12]. We initialize the superconducting pairing potential $\Delta(\mathbf{r})$ in the *super-*
91 *conducting strength representation*. In this approach, the pairing potential is expressed, in real
92 space, via a superconducting strength parameter $\bar{\Delta}$.

93 In ML FeSe, we initialize $\Delta(\mathbf{r})$ with spheres centered on the Fe atoms, each with $\bar{\Delta} = 15$ meV
94 [Fig. 1.(a)]. The BdG spectrum [Fig. 1.(b, c)], the SC–DOS $\rho(\varepsilon)$ and anomalous DOS $\chi(\varepsilon)$
95 [Fig. 1.(d)] reveal several superconducting gaps/coherence peaks at energies ±1.8 (Δ_1), ±5
96 (Δ_2), and ±6.4 meV (Δ_3). The orbital projected SC–DOS [Fig. 1.(f)] shows that the supercon-
97 ducting states are mostly dominated by the Fe $3d_{z^2}$ and, to a minor extent, by $3d_{xz}$ and $3d_{yz}$

orbitals. We identify the nature of the coherence peaks from the superconducting [Fig. 1.(d)] and orbital-projected normal state (Fig.2) band structures: The Δ_1 coherence peaks originate from Fe d_{z^2} along $X - M$ (close to M) and to d_{xz}/d_{yz} along $\Gamma - X$ [Figs. 2.(a, b, c)]. Δ_2 originates from Fe d_{xz} and d_{yz} along $M - \Gamma$ close to M [Fig. 2.(a, b)]. Δ_3 originates from Fe d_{z^2} along $\Gamma - M$ close to Γ [Fig. 2.(c)]. The Δ_1 and Δ_2 peaks exhibit strong electron-hole coupling, as evidenced by the band inversion between electrons (red) and holes (blue) at the corresponding gap [Fig. 1.(d)]. From the band structure, we observe a strong anisotropy in the momentum-resolved superconducting gap structure, i.e., $\Delta(\mathbf{k}_1) \neq \Delta(\mathbf{k}_2)$. We note that the type of Fe orbitals associated with superconductivity and the nature of superconductivity in bulk FeSe differs from ML FeSe: We have recently showed [12] that the superconducting gap of bulk FeSe is V-shaped, and is due to Fe d_{xz} and d_{yz} only, in agreement with experiments [20]. FeSe ML, instead, features a U-shaped gap with multiple coherence peaks, mostly due to d_{z^2} and, in minor part, to d_{xz} and d_{yz} orbitals.

FeSe/STO exhibits three pronounced peaks at ± 8 (Δ_1), ± 14.3 (Δ_2), and ± 20 meV (Δ_3) in the SC–DOS [Fig. 3.(e)]. The superconducting band structure [Fig. 3.(d)] shows several gaps of different sizes near M, along the $M - X$ and $M - \Gamma$ directions, demonstrating that $\Delta(\mathbf{k})$ is anisotropic. The normal-state band structure [Fig. 3.(b)] and the projected SC–DOS [Fig. 3.(g)] allow us to attribute the Δ_1 and Δ_2 peaks/gaps to the STO substrate and, more specifically, to the interfacial O p_x and p_y states [Figs. 15.(g,h)]. Therefore, we deduce that superconductivity has been induced by proximity on the oxygen atoms. The Δ_3 peak is, instead, due to Fe and originates along the $M - \Gamma$ line close to M. By comparing with FeSe ML, we deduce that the Fe-related SC-gap at M broadens and changes in orbital character from d_{z^2} to d_{xz} and d_{yz}, [Fig. 3.f] in FeSe/STO due to coupling with the substrate. The hybridization between FeSe and the substrate, combined with particle-hole symmetry, leads to the emergence of new bands in the BdG spectrum [Figs. 3.(c,d)] that are not present in the normal state dispersion [Figs. 3.(b)]. These new bands are at Γ (~ 250 meV below E_F), and M (~ 15–30, 70 and ~ 180 meV below E_F) originating from the hybridization of Fe d_{z^2} and O p_z (at Γ) and Fe d_{xz} and d_{yz} with O p_x and p_y (at M). The energy range of these bands corresponds to the experimentally observed "replica bands" [21]. In our simulations, replica bands originate from: (i) the superconducting pairing potential which couples the interfacial region between FeSe and STO, and (ii) particle-hole symmetry which mirrors the normal-state conduction states in the valence manifold. Our results qualitatively agree with ARPES measurements of FeSe/STO [1, 2, 8]. Differences might be due to the semi-phenomenological nature of the SIESTA–BdG method: the initialization of the pairing potential results in an energy shift of the coherence peaks (Appendix B).

3   Conclusion

In this study, we investigated the superconducting properties of ML FeSe, employing a combined Kohn–Sham and Bogoliubov–de Gennes approach. We analyzed two cases: freestanding FeSe (ML FeSe) and FeSe on a TiO$_2$–terminated STO substrate (FeSe/STO).

For both systems, we predicted an anisotropic superconducting gap $\Delta(\mathbf{k})$ [Figs. 3.(d) and 1.(d)]. We identified the nature of the superconducting coherence peaks and attributed their origin to specific regions in the Brillouin Zone: In freestanding FeSe, superconductivity is due to states around Γ and M points. In FeSe/STO, superconductivity originates from states around the M point only.

In addition, we identified the specific atoms and orbitals that are responsible for superconductivity: We observed a change in the orbital character of the Fe states responsible for superconductivity from d_{z^2} (ML FeSe) to d_{xy}/d_{yz} (FeSe/STO). In FeSe/STO, Fe d and O p

145 orbitals strongly hybridize near the Fermi energy at the M point [Figs. 3.(b)] giving rise to
146 two coherence peaks ($\Delta_{1/2}$, mostly contributed by O) and a higher-energy one (Δ_3, mostly
147 contributed by Fe). Remarkably, we observed proximity-induced superconductivity in the in-
148 terfacial TiO_2 layer.

149   Our analysis of the normal-state band structure of the two materials allowed us to shed light
150 on the different mechanisms behind their superconductivity: In ML FeSe, metallicity originates
151 from an electron pocket at M and a hole pocket along the $\Gamma - X$ line. In FeSe/STO, instead,
152 the hole pocket shifts to lower energies in the valence band. Therefore, the superconducting
153 mechanism is intrinsically different in two cases: In ML FeSe, Cooper pairs can either form at
154 $\sim \Gamma$ and $\sim M$ (difference between electron and hole crystal momentum $Q = 0$), or can scatter
155 between M and Γ ($Q \neq 0$). In FeSe/STO, instead, Cooper pairs formation is only possible at
156 M ($Q = 0$).

157   In both ML FeSe and FeSe/STO, we found multiple competing magnetic configurations. In
158 this work, we focused on the checkerboard antiferromagnetic phase because its band structure
159 best resembles ARPES measurements [18]. The impact of different magnetic configurations
160 on the superconducting phase remains an open question, with the possibility that supercon-
161 ductivity may be favored in a specific direction when using the single stripe configuration with
162 different spin alignments along the x and y axes. Future studies could investigate the super-
163 conducting state under different magnetic configurations to provide deeper insights into its
164 behavior, or explore the potential for topological superconductivity in FeSe systems coupled
165 with magnetic impurities and strong spin-orbit coupling, such as the recently observed zero
166 energy states at the edges of line defects in Fe(Se, Te) [22].

167   Our findings emphasize the role of hybridization with the substrate in determining the
168 superconducting properties of FeSe. Hybridization between Fe and the substrate triggers
169 proximity-induced superconductivity in STO. We suggest that heterostructures consisting of
170 FeSe and substrates, including elements with high electron affinity, will promote charge trans-
171 fer and facilitate Cooper pair formation in the substrate, opening the way to engineering novel
172 FeSe-based superconductors operating at high temperatures.

4 Methods

4.1 First-principles ground state simulations

175 All simulations were performed using the SIESTA method [13, 23], with the PBE [24] func-
176 tional, norm-conserving pseudopotentials from the Pseudo-Dojo database [25], and the default
177 SIESTA double-ζ polarized (DZP) basis set with an orbital cutoff radii of 272 meV. Simulations
178 were converged for a mesh–cutoff of 1300 Ry. In FeSe/STO we account for the correlation
179 effects between Fe and the interfacial oxygen atoms by applying a Hubbard correction U of
180 0.1 eV to the Fe d states [26, 27]. This value of U allows us to reproduce reasonably the band
181 dispersion observed in ARPES [3, 17], in particular the position of the highest occupied state
182 at Γ, as illustrated in Fig. 14). All calculations include SOC.

183   To solve the KS-equations, we employed a $101 \times 101 \times 1$ and $16 \times 16 \times 1$ **k**-grid for ML FeSe
184 and FeSe/STO, respectively. The Fermi-Dirac occupation function was smoothed out using an
185 electronic temperature of 10 meV in the normal state for both freestanding FeSe and FeSe/STO.
186 This value has been lowered to 0.1 meV for the superconducting state simulations to ensure
187 that the broadening of the electronic states is well below the size of the superconducting gap.
188 The crystal structures were relaxed with a maximum force tolerance of 0.005 eV/Å.

4.2 SIESTA-BdG method

The superconducting properties were modeled using the SIESTA–BdG method [12]. In this approach, a semi-empirical superconducting pairing potential is introduced on top of the self-consistent Kohn-Sham Hamiltonian describing the normal state. We used the *fixed–Δ* method with the superconducting pairing potential initialized in real space (*superconducting strength representation*) as touching spherical hardwells. We used hardwells with radius $\mathbf{r} = 1.32$ Å ($\mathbf{r} = 1.39$ Å) and strength $\bar{\Delta} = 15.0$ meV ($\bar{\Delta} = 73.0$ meV) around the Fe atoms for ML FeSe (FeSe/STO). We used a radius of $\mathbf{r} = 1.5$ Å and $\bar{\Delta} = 11.0$ meV for the interfacial oxygen atoms. For a discussion on the initialization of different pairing potential see Supporting Information B.The superconducting DOS were sampled with a uniform $350 \times 350 \times 1$ and $301 \times 301 \times 1$ **k**-grid, and refined with one iteration of the adaptive-grid scheme with a $3 \times 3 \times 1$ subgrid for ML FeSe and FeSe/STO, respectively.

Acknowledgements

The authors acknowledge the fruitful discussion with Ingmar Swart, Samir Lounis, and Eberhard K. U. Gross.

Author contributions   R. Reho and N. Wittemeier contributed equally to this work.

Funding information   ZZ acknowledges the research program "Materials for the Quantum Age" (QuMat) for financial support. This program (registration number 024.005.006) is part of the Gravitation program financed by the Dutch Ministry of Education, Culture and Science (OCW).This project has received funding from the European Union's Horizon Europe research and innovation program under Grant Agreement No 101130384 (QUONDENSATE). RR and AK acknowledges financial support from Sector Plan Program 2019-2023. NW acknowledges support from the EU MaX CoE (Grant No. 101093374) and Grants No. PCI2022-134972-2 and PID2022-139776NB-C62 funded by the Spanish MCIN/AEI/10.13039/501100011033 and by the ERDF, A way of making Europe. NW further acknowledges funding from the European Union's Horizon 2020 research and innovation programme under the Marie Skłodowska-Curie Grant Agreement No. 754558 (PREBIST – COFUND). ICN2 is supported by the Severo Ochoa programme from Spanish MINECO (Grant no. CEX2021-001214-S) and by Generalitat de Catalunya (CERCA program and Grant No. 2021SGR01519). This work was sponsored by NWO-Domain Science for the use of supercomputer facilities. We also acknowledge that the results of this research have been achieved using the Tier-0 PRACE Research Infrastructure resource Discoverer based in Sofia, Bulgaria (OptoSpin project id. 2020225411).

A   Magnetic order

Over the last decade, the ground state of FeSe has been hotly debated in the literature. Magnetic frustration and spin fluctuations make it difficult to describe this system with the Heisenberg or Ising models. Recently, *Glasbrenner et al.* [14] performed a detailed analysis, based both on first principles and model calculations establishing the Staggered Dimer (SD) as the most stable configuration for this system. Our first-principles *ab-initio* analysis confirms their result. In Fig. 4 we show the computed total energies for the Single Stripe (SS), Staggered Trimer (ST), Staggered Dimer, in-plane (IP) and out-of-plane (OOP) CheckerBoard (CB), FerroMagnetic (FM) and non magnetic (NM) configurations. We report the difference in total

energies ΔE with respect to the ground state (E_{min}) in Fig.s 4 and 5 and Table 1.

Two different basis sets were tested: Double-Zeta Polarized (DZP) with orbital-confining cutoff radii (PAO.EnergyShift) of 272 meV and 25 meV. The first choice leads to physically correct energetic ordering, and therefore our calculations are performed with this basis set.

The low-energy magnetic configurations for ML FeSe are ST, SS, and SD, with the ST only 0.231 meV below the SD. This energy difference is below the 0.5 meV/Fe accuracy of our simulations, hence, we conclude that the three configurations are iso–energetic. We report our results in Fig. 5 and Table 1.

Table 1: Difference in total energies $\Delta E = E - E_{\min}$, of ML FeSe and FeSe/STO with different magnetic configurations. The minimal energies are highlighted in bold.

ML FeSe	$\Delta E[meV]$
SS	8.868
ST	**0.000**
SD	0.231
CB IP	68.453
CB OOP	68.557
FM	166.314
NM	166.357

Bulk FeSe	$\Delta E[meV]$
SS	9.418
ST	0.424
SD	**0.000**
CB	65.846
FM	238.971
NM	241.511

B Initialization of the Pairing Potential and Its Impact on the Superconducting Properties

In the SIESTA-BdG method, one can employ different approaches for solving the BdG equations and initializing the pairing potential Δ [12]. We explored multiple initialization schemes for the pairing potential in both ML FeSe and FeSe/STO. In the main text, we focus on results obtained using the *fixed–Δ* method to solve the SIESTA-BdG equations, initialized within the *superconducting strength representation*. The *fixed–Δ* algorithm solves the Bogoliubov–de Gennes equations ensuring self-consistency in the normal Hamiltonian and density while holding Δ constant during the SIESTA–BdG scf steps. At every scf step the normal state Hamiltonian, the normal and the anomalous densities are updated. The *superconducting strength representation* initializes Δ in real space by specifying an initial guess for the pairing strength, $\bar{\Delta}$ (when no risk of confusion arise, we simply write Δ).

For ML FeSe, we analysed the shape and magnitude of the SC–DOS $\rho(\varepsilon)$ while varying the initial value of $\bar{\Delta}$. As shown in Fig. 6, $\rho(\varepsilon)$ is zero for $\bar{\Delta} = 0$, indicating the absence of superconductivity. A transition from a non-gapped to fully gapped SC–DOS occurs as $\bar{\Delta}$ increases from 3 to 5 meV. Namely, $\bar{\Delta} < 5$ meV is too small to describe superconductivity in ML FeSe. For $\bar{\Delta} = 5$ meV, the double peaks around ±8 meV merge into a single peak. Further increases in $\bar{\Delta}$ result in broader coherence peaks, reflecting the enhanced value of the superconducting pairing potential. Experimentally, different values for the superconducting

gap width have been reported, with $\bar{\Delta} = 15$ meV in [8]. The BdG spectrum and SC–DOS (Figs. 7 and 6) does not, qualitatively, change for $\bar{\Delta}$ close to 15 meV. Therefore, we employed $\bar{\Delta} = 15$ meV for the SIESTA-BdG simulations presented in the main text.

For FeSe/STO, the interpretation of the SC–DOS is more complex. Our results indicate that only the states near the FeSe/STO interface contribute significantly to $\rho(\varepsilon)$ close to the Fermi level, regardless of the spatial initialization of the pairing potential. In order to assess this stament, we first initialize the pairing potential $\bar{\Delta}$ uniformly across the unit cell (Fig. 9) with values ranging from 0 to 24 meV. The SC–DOS is metallic for $\bar{\Delta} = 0$. As $\bar{\Delta}$ increases , two peaks are clearly distinguishable and their separation widens. At $\bar{\Delta} = 0$ meV, we observe a pair of coherence peaks at ± 4.5 meV, which we attribute to the gaps in flat degenerate bands near the Fermi level in the normal state of FeSe/STO [Fig. 3.(b)]. These peaks primarily orginate from Fe d orbitals. As $\bar{\Delta}$ increases, a second pair of coherence peaks emerges starting at $\bar{\Delta} = 6$ meV. This second pair, associated with interfacial O p–orbitals, becomes broader with increasing $\bar{\Delta}$, while the first pair remains unchanged. Thus, the constant initialization of the pairing potential indicates that both Fe and oxygen play a role in the superconducting coupling, although the exact peak positions are not quantitatively accurate. Furthermore, the SC–DOS does not completely drop to zero regardless of the value of $\bar{\Delta}$ while the anomalous DOS does. We interpret this behavior as follows: the first pair of coherence peaks arises from intrinsic electronic properties (coupling to STO), while the second is driven by the superconducting pairing potential, as evidenced by the trends in $\chi(\varepsilon)$. The BdG spectrum near the high–symmetry point M (Fig. 8) provides further insights. Along the $M - X'$ path (left) and the $M - X$ path (right), we observe a widening separation between electron and hole states as $\bar{\Delta}$ increases, except for states near the Fermi level. Notably, a gap–closing feature appears along the $M - X'$ path, which is absent along $M - X$. This suggests a breaking of inversion symmetry in the system. A value of $\bar{\Delta} = 24$ meV is not sufficient to fully open the gap for FeSe/STO. Our tests indicate that at least a value of 45 meV is needed. For the reasonings above, we initialized the pairing potential $\bar{\Delta}$ only on the Fe atoms of the ML and the interfacial oxygen atoms. We tested that, qualitatively, no differences arise if the superconducting pairing potential is initialized uniformly across the unit cell or only on the Fe and interfacial Oxygen atoms. We also tested the case where the superconducting pairing potential is initialized as touching spheres on the Fe atoms (Fig. 10).

For FeSe/STO, we report the SC–DOS and anomalous DOS for different values of $\bar{\Delta}$ from 0 meV up to 300 meV, with the superconducting pairing initialized on the Fe interfacial oxygen atoms (Fig.s 11 and 12). These results show that for a higher value $\bar{\Delta}$ the SC–DOS becomes gapped.

C Supplementary Electronic Structure Analysis of ML FeSe and FeSe/STO

In this section, we present supplementary figures that support the discussion in the main text. We compute the orbital-projected band structure of ML FeSe (Fig. 13) and FeSe/STO (Fig. 15). We show the Fermi surfaces of ML FeSe and FeSe/STO (Fig. 16). We examine the changes in the electronic dispersion of FeSe/STO as a function of the Hubbard U parameter (Fig. 14). We compare our results with ARPES data [8] and employ a value of $U = 0.1$ eV for the simulations performed in the main text.

References

[1] Q.-Y. Wang, Z. Li, W.-H. Zhang, Z.-C. Zhang, J.-S. Zhang, W. Li, H. Ding, Y.-B. Ou, P. Deng, K. Chang *et al.*, *Interface-induced high-temperature superconductivity in single unit-cell fese films on srtio3*, Chinese Physics Letters **29**(3), 037402 (2012).

[2] D. Huang and J. E. Hoffman, *Monolayer fese on srtio3*, Annual Review of Condensed Matter Physics **8**, 311 (2017).

[3] W. Zhang, Z. Li, F. Li, H. Zhang, J. Peng, C. Tang, Q. Wang, K. He, X. Chen, L. Wang *et al.*, *Interface charge doping effects on superconductivity of single-unit-cell fese films on srtio 3 substrates*, Physical Review B **89**(6), 060506 (2014).

[4] F. Zheng, Z. Wang, W. Kang and P. Zhang, *Antiferromagnetic fese monolayer on srtio3: the charge doping and electric field effects*, Scientific reports **3**(1), 2213 (2013).

[5] A. I. Coldea and M. D. Watson, *The key ingredients of the electronic structure of fese*, Annual Review of Condensed Matter Physics **9**(1), 125 (2018).

[6] Z. Wei, S. Li, B. Liu, X. Sun, Y. Hu, S. Sun, S. Peng, Y. Luo, L. Huai, J. Shen *et al.*, *Particle-hole mixed bogoliubov quasiparticles and cooper instability in single-unit-cell fese/srtio3 films*, Communications Materials **5**(1), 118 (2024).

[7] Y. Zhang, J. Lee, R. Moore, W. Li, M. Yi, M. Hashimoto, D. Lu, T. Devereaux, D.-H. Lee and Z.-X. Shen, *Superconducting gap anisotropy in monolayer fese thin film*, Physical review letters **117**(11), 117001 (2016).

[8] X. Liu, L. Zhao, S. He, J. He, D. Liu, D. Mou, B. Shen, Y. Hu, J. Huang and X. Zhou, *Electronic structure and superconductivity of fese-related superconductors*, Journal of Physics: Condensed Matter **27**(18), 183201 (2015).

[9] S. Acharya, D. Pashov, F. Jamet and M. van Schilfgaarde, *Electronic origin of t c in bulk and monolayer fese*, Symmetry **13**(2), 169 (2021).

[10] S. Acharya, D. Pashov and M. Van Schilfgaarde, *Role of nematicity in controlling spin fluctuations and superconducting t c in bulk fese*, Physical Review B **105**(14), 144507 (2022).

[11] S. Acharya, M. I. Katsnelson and M. van Schilfgaarde, *Vertex dominated superconductivity in intercalated fese*, npj Quantum Materials **8**(1), 24 (2023).

[12] R. Reho, N. Wittemeier, A. H. Kole, P. Ordejón and Z. Zanolli, *Density functional bogoliubov-de gennes theory for superconductors implemented in the siesta code*, Phys. Rev. B **110**, 134505 (2024), doi:10.1103/PhysRevB.110.134505.

[13] A. Garcia, N. Papior, A. Akhtar, E. Artacho, V. Blum, E. Bosoni, P. Brandimarte, M. Brandbyge, J. I. Cerdá, F. Corsetti *et al.*, *Siesta: Recent developments and applications*, The Journal of chemical physics **152**(20), 204108 (2020).

[14] J. K. Glasbrenner, I. I. Mazin, H. O. Jeschke, P. J. Hirschfeld, R. M. Fernandes and R. Valentí, *Effect of magnetic frustration on nematicity and superconductivity in iron chalcogenides*, Nature Physics **11**(11), 953 (2015), doi:10.1038/nphys3434.

[15] A. Ghosh, P. Chudzinski and M. Grüning, *First-principles study and mesoscopic modeling of two-dimensional spin and orbital fluctuations in fese*, Physical Review Research **6**(4), 043154 (2024).

[16] P. Chudzinski, A. Ghosh and M. Gruening, *Generalized incommensurability: the role of anomalously strong spin-orbit coupling for the spin ordering in a quasi-2d system, fese*, arXiv preprint arXiv:2503.16016 (2025).

[17] Q. Wang, Y. Shen, B. Pan, X. Zhang, K. Ikeuchi, K. Iida, A. Christianson, H. Walker, D. Adroja, M. Abdel-Hafiez *et al.*, *Magnetic ground state of fese*, Nature communications **7**(1), 12182 (2016).

[18] Z. Wang, H. Zhang, D. Liu, C. Liu, C. Tang, C. Song, Y. Zhong, J. Peng, F. Li, C. Nie *et al.*, *Topological edge states in a high-temperature superconductor fese/srtio3 (001) film*, Nature materials **15**(9), 968 (2016).

[19] R. S. Mulliken, *Electronic population analysis on lcao–mo molecular wave functions. i*, The Journal of chemical physics **23**(10), 1833 (1955).

[20] S. Kasahara, T. Watashige, T. Hanaguri, Y. Kohsaka, T. Yamashita, Y. Shimoyama, Y. Mizukami, R. Endo, H. Ikeda, K. Aoyama *et al.*, *Field-induced superconducting phase of fese in the bcs-bec cross-over*, Proceedings of the National Academy of Sciences **111**(46), 16309 (2014).

[21] J. Lee, F. Schmitt, R. Moore, S. Johnston, Y.-T. Cui, W. Li, M. Yi, Z. Liu, M. Hashimoto, Y. Zhang *et al.*, *Interfacial mode coupling as the origin of the enhancement of t c in fese films on srtio3*, Nature **515**(7526), 245 (2014).

[22] C. Chen, K. Jiang, Y. Zhang, C. Liu, Y. Liu, Z. Wang and J. Wang, *Atomic line defects and zero-energy end states in monolayer Fe(Te,Se) high-temperature superconductors*, Nature Physics **16**(5), 536 (2020), doi:10.1038/s41567-020-0813-0, Publisher: Nature Publishing Group.

[23] J. M. Soler, E. Artacho, J. D. Gale, A. García, J. Junquera, P. Ordejón and D. Sánchez-Portal, *The siesta method for ab initio order-n materials simulation*, Journal of Physics: Condensed Matter **14**(11), 2745 (2002).

[24] J. P. Perdew, K. Burke and M. Ernzerhof, *Generalized gradient approximation made simple*, Physical review letters **77**(18), 3865 (1996).

[25] M. J. van Setten, M. Giantomassi, E. Bousquet, M. J. Verstraete, D. R. Hamann, X. Gonze and G.-M. Rignanese, *The pseudodojo: Training and grading a 85 element optimized norm-conserving pseudopotential table*, Computer Physics Communications **226**, 39 (2018).

[26] A. Liechtenstein, V. I. Anisimov and J. Zaanen, *Density-functional theory and strong interactions: Orbital ordering in mott-hubbard insulators*, Physical Review B **52**(8), R5467 (1995).

[27] E. Bousquet and N. Spaldin, *J dependence in the lsda+u treatment of noncollinear magnets*, Physical Review B—Condensed Matter and Materials Physics **82**(22), 220402 (2010).
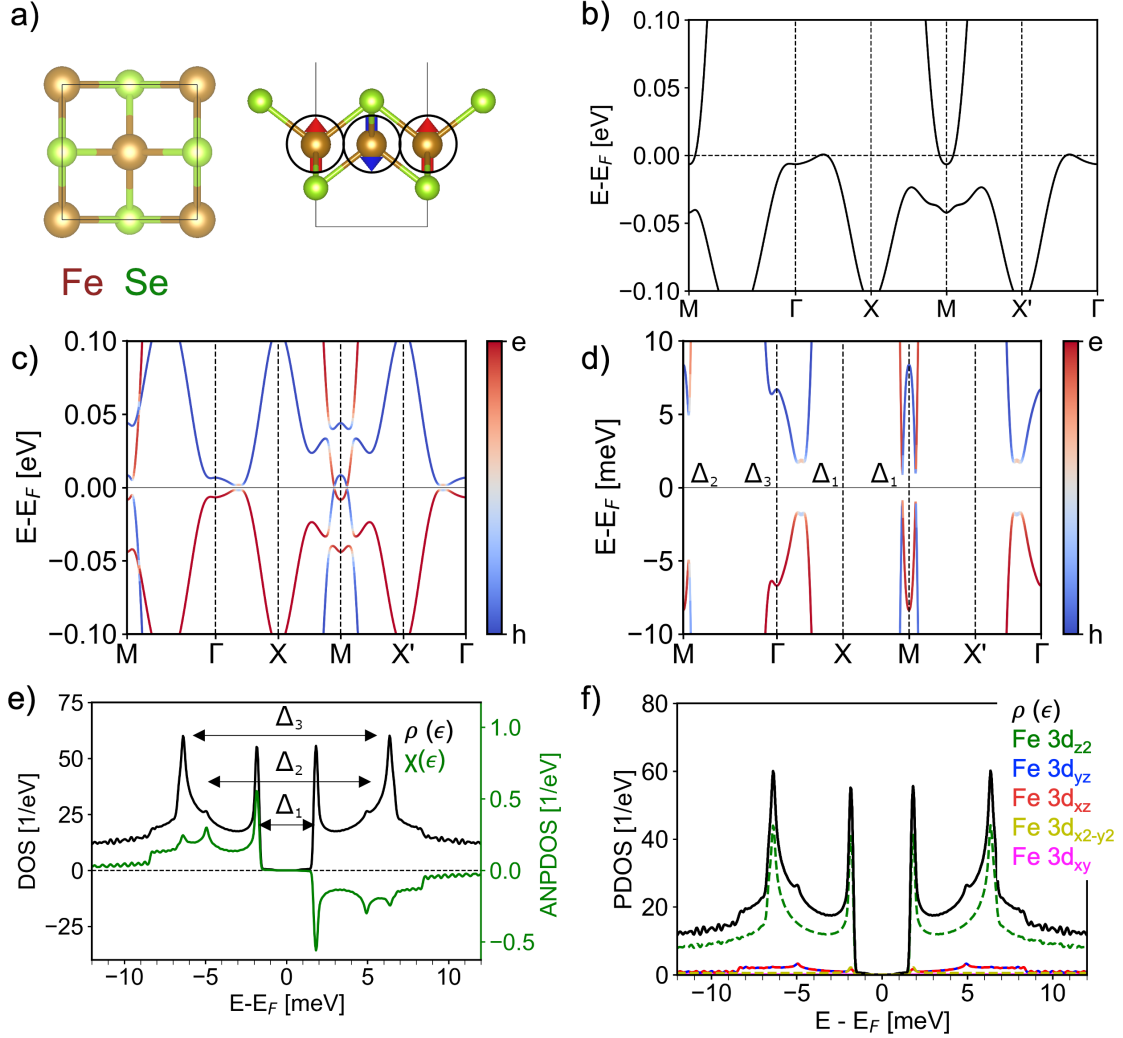
Figure 1: ML FeSe in the CB-AFM magnetic phase. (a) Top and side view of a unit cell of ML FeSe, with red and blue arrows representing spin directions and black circles illustrating the initialization of the superconducting pairing potential. (b) Normal state band structure. (c) Superconducting band structure projected on the electron (red) and hole (blue) components of the BdG spectrum. In (d) we report a narrower energy range around the SC gap. (e) SC–DOS ($\rho(\varepsilon)$, black) and anomalous SC–DOS ($\chi(\varepsilon)$, green) exhibiting superconducting gaps with widths $\Delta_1 = 3.6$, $\Delta_2 = 10.0$, and $\Delta_3 = 12.8$ meV. (f) SC–DOS projected over Fe orbitals.
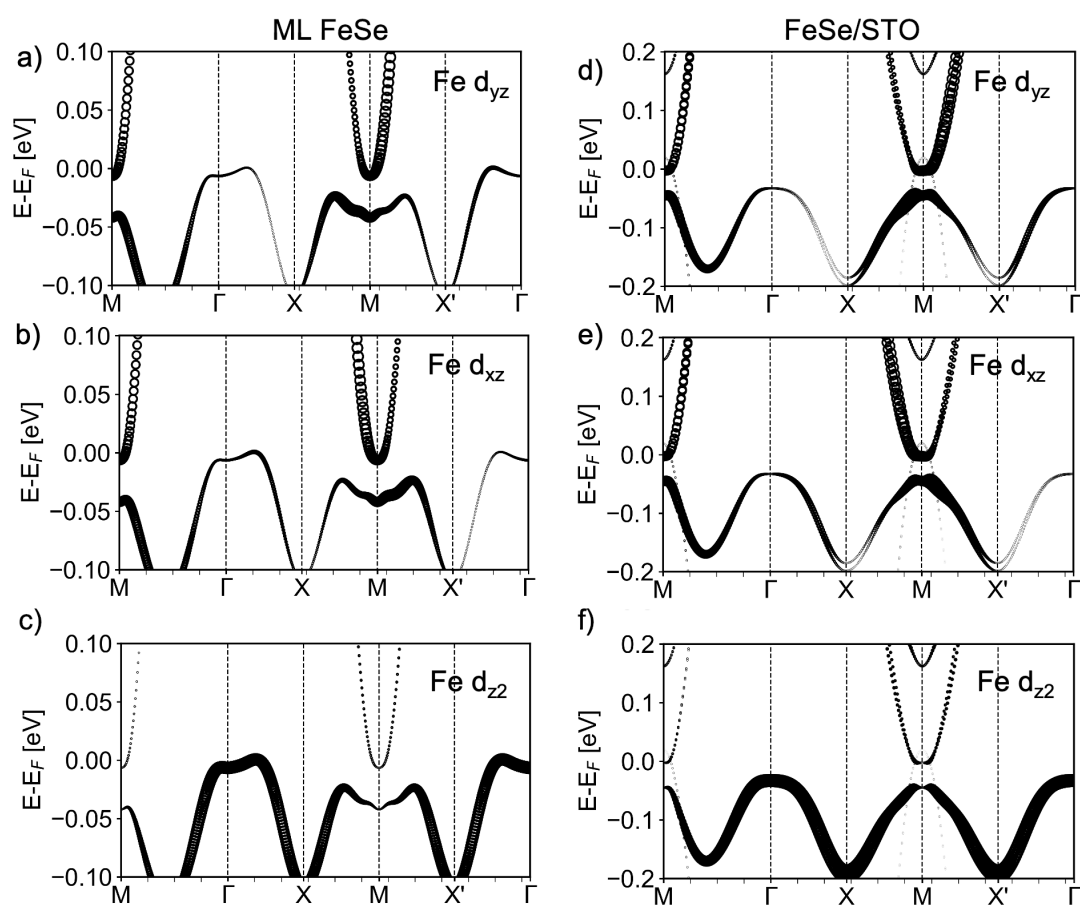
Figure 2: Normal state electronic band structures of (a-c) FeSe ML and (d-f) FeSe/STO projected on selected Fe orbitals. The projection over all orbitals is reported in Appendix Figs. 13 and 15
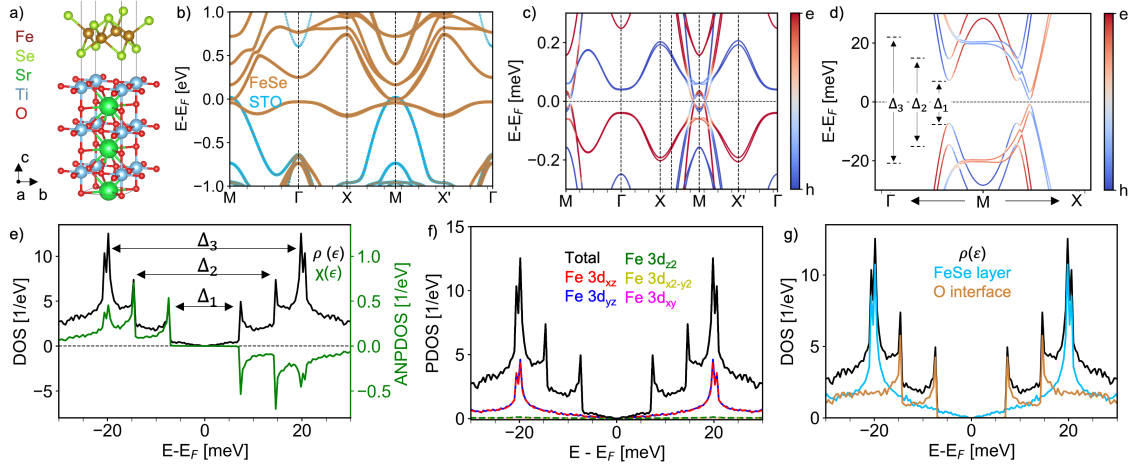
Figure 3: FeSe/STO with a TiO$_2$–terminated surface, FeSe is in the checkerboard AFM magnetic phase: (a) atomistic model (side view). (b) Electronic band structure projected on FeSe (light brown) and STO (light blue). (c,d) Superconducting band structure in two different energy ranges. The color scheme highlights contributions from electron-like (red) and hole-like (blue) components of the BdG spectrum. (e) SC–DOS ($\rho(\varepsilon)$, black) and anomalous SC–DOS ($\chi(\varepsilon)$, green) with superconducting gap widths $\Delta_1 = 16.0$, $\Delta_2 = 28.6$, and $\Delta_3 = 40.0$ meV. (f,g) Total (black) and projected SC–DOS over (f) orbitals, and (g) FeSe layer (light brown) and interfacial O atoms (light blue).
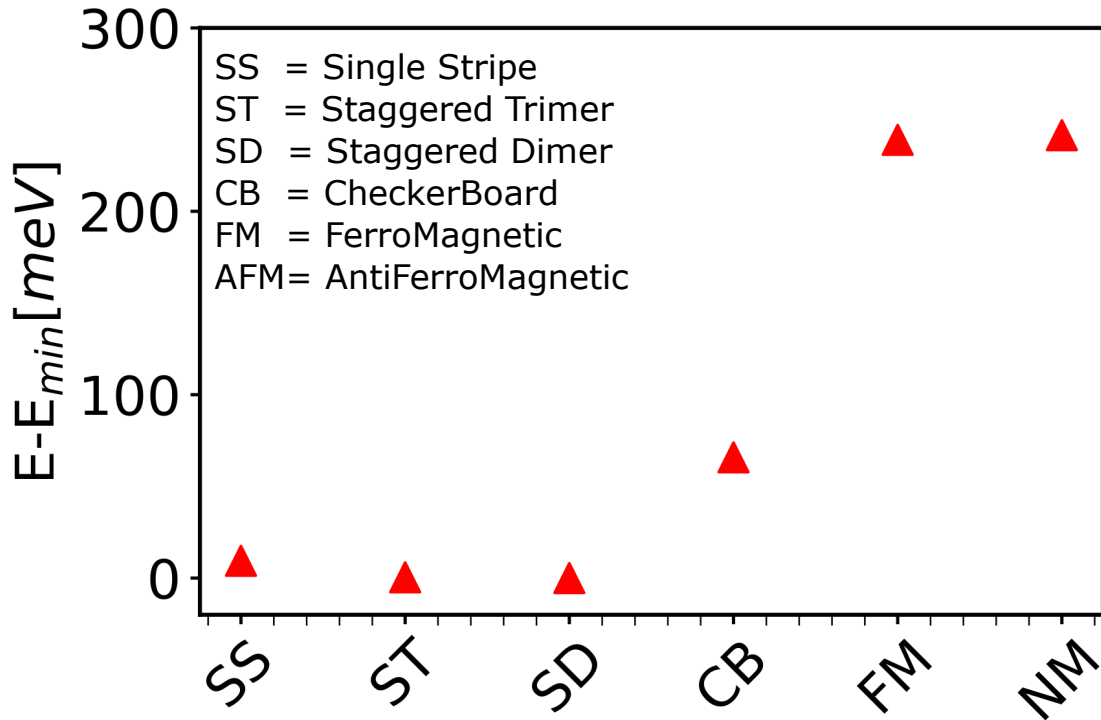
Figure 4: Energetic magnetic ordering for FeSe bulk. The lowest energy magnetic state is the Staggered Dimer configuration.
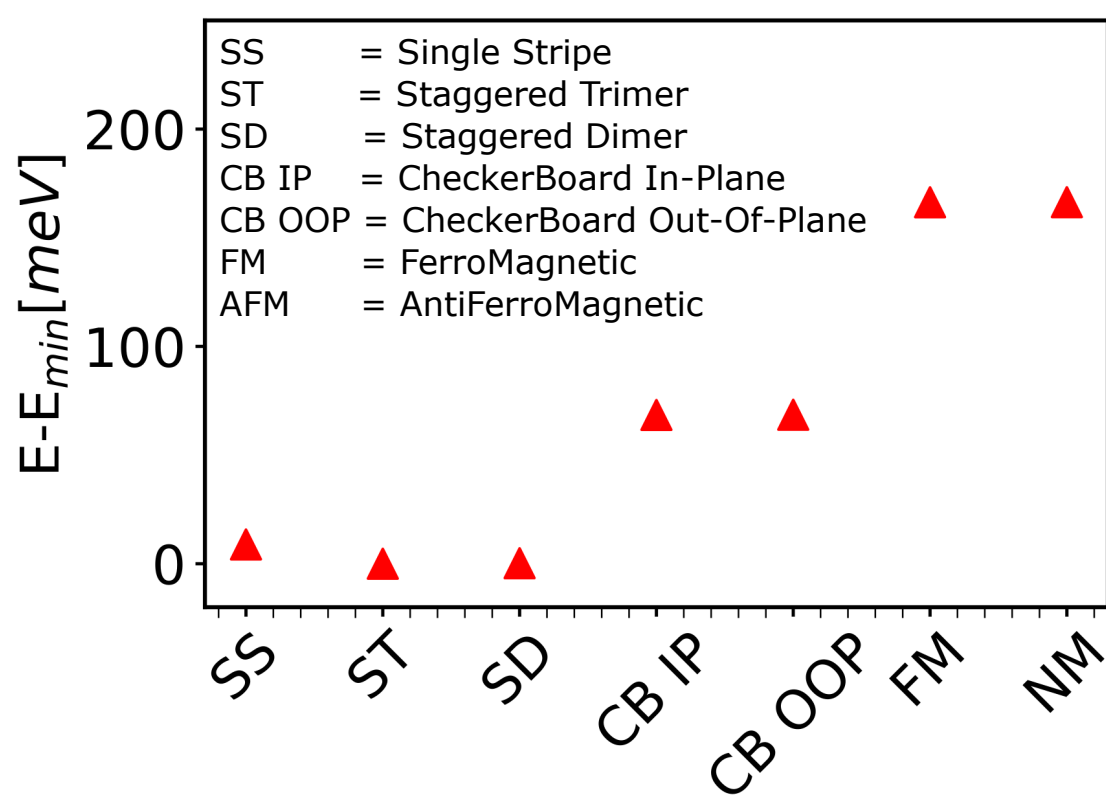
Figure 5: Energetic magnetic ordering for ML FeSe.
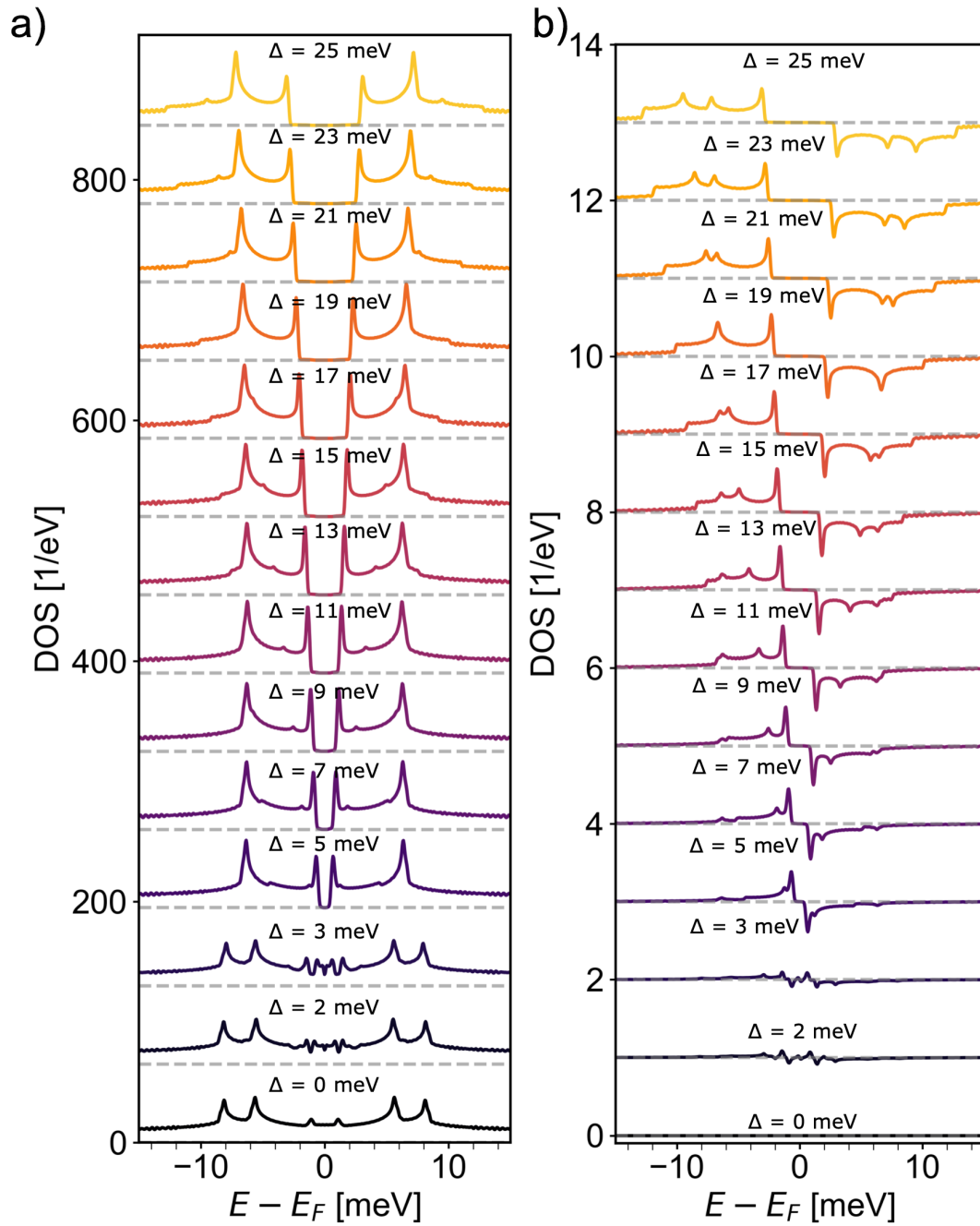
Figure 6: (a) SC–DOS and (b) anomalous DOS (right) for ML FeSe varying the initial value of Δ from 0 to 25 meV. The superconducting pairing potential is initialized only on the Fe atoms.
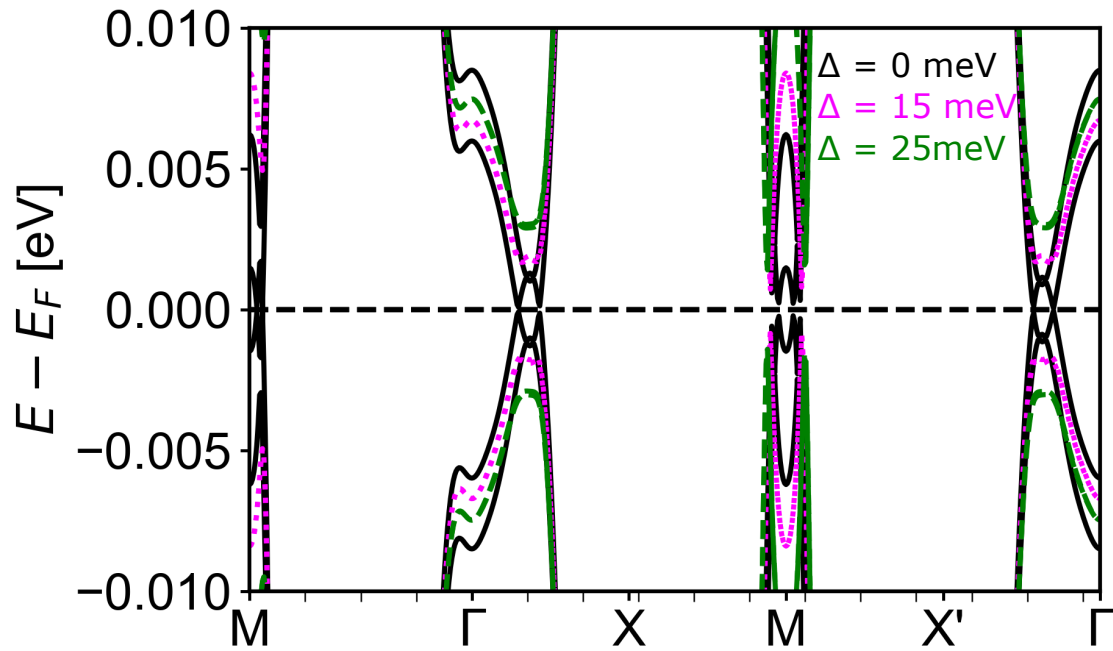
Figure 7: Superconducting band structure of ML FeSe with $\Delta = 0$ (black), 15 (magenta), or 25 (green) meV. The superconducting pairing potential is initialized only on the Fe atoms.
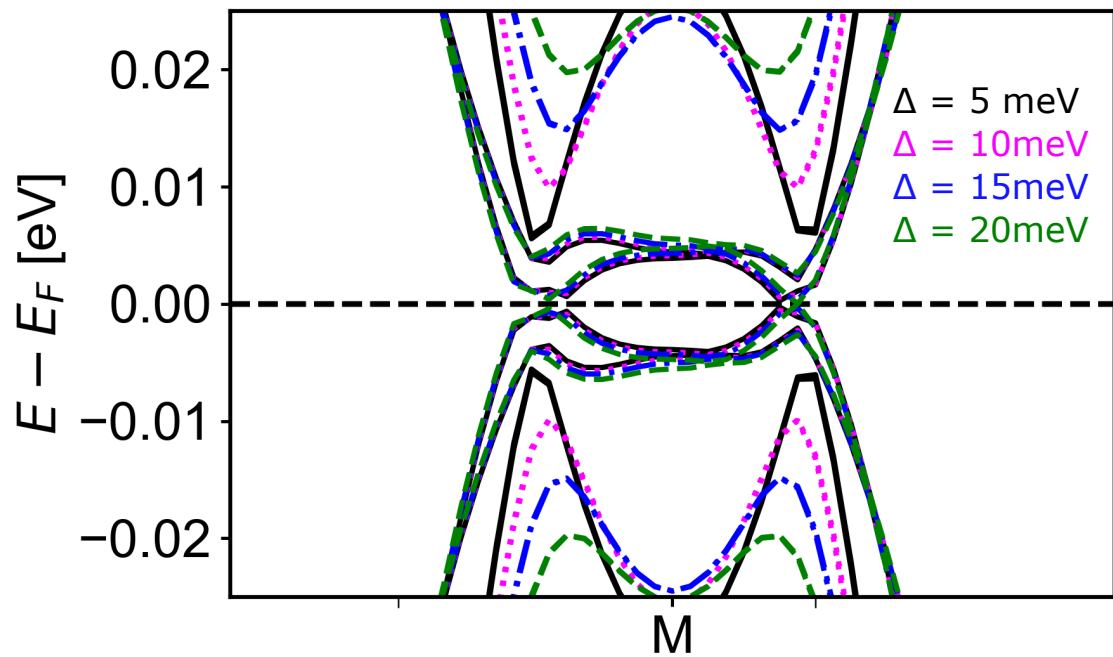
Figure 8: Superconducting band structure of FeSe/STO with $\Delta = 0$ (black), 10 (magenta), 15 (blue), or 20 (green) meV. The superconducting pairing potential is initialized on the Fe atoms and the oxygen atoms of the TiO_2 terminated surface.
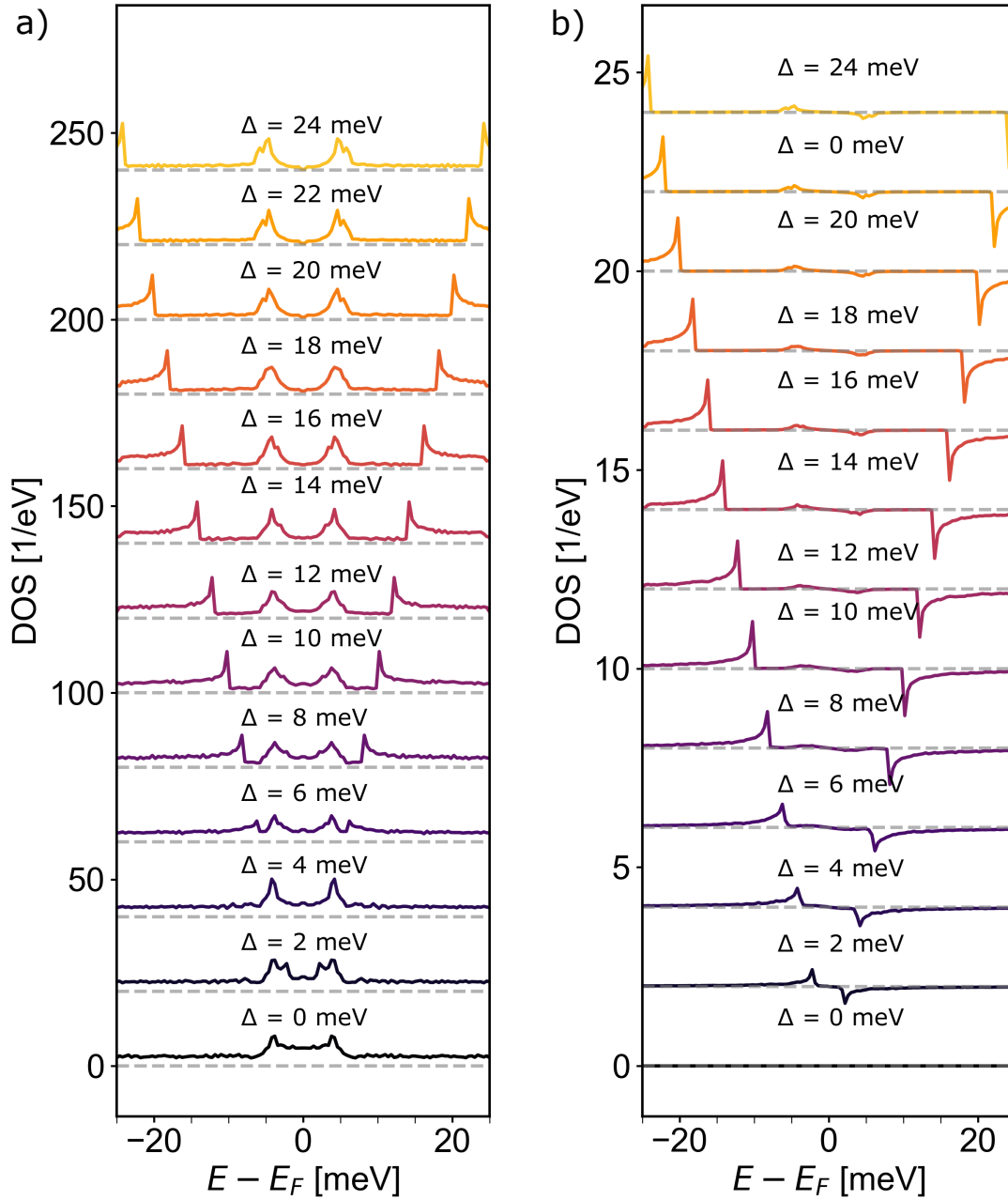
Figure 9: (a) SC–DOS and (b) anomalous DOS (right) for FeSe/STO obtained by varying Δ from 0 meV to 24 meV. The superconducting pairing potential is initialized in the whole unit cell with a constant value.
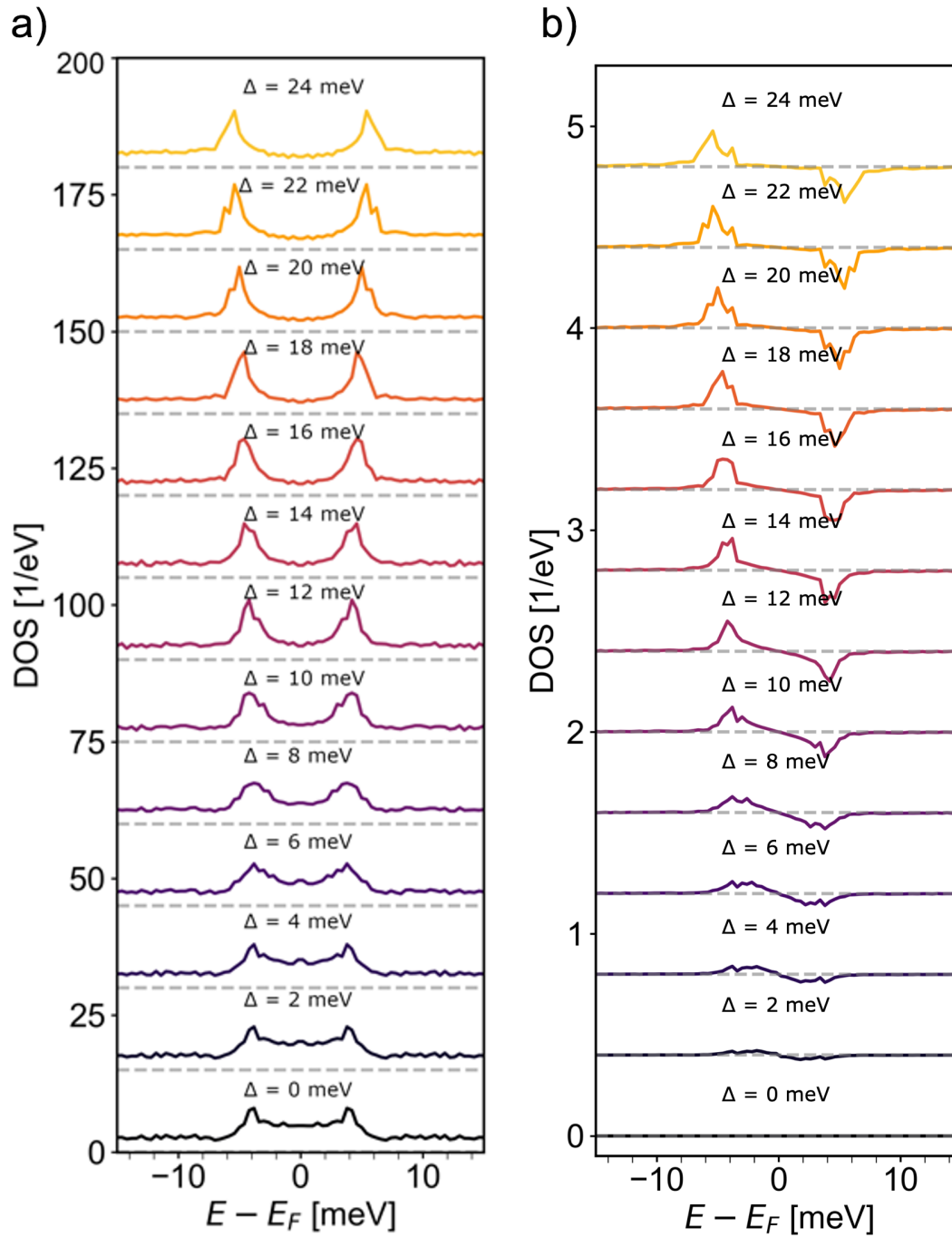
Figure 10: (a) SC–DOS and (b) anomalous DOS (right) for FeSe/STO by obtained by varying Δ from 0 to 24 meV. The superconducting pairing potential is initialized only on the Fe atoms.
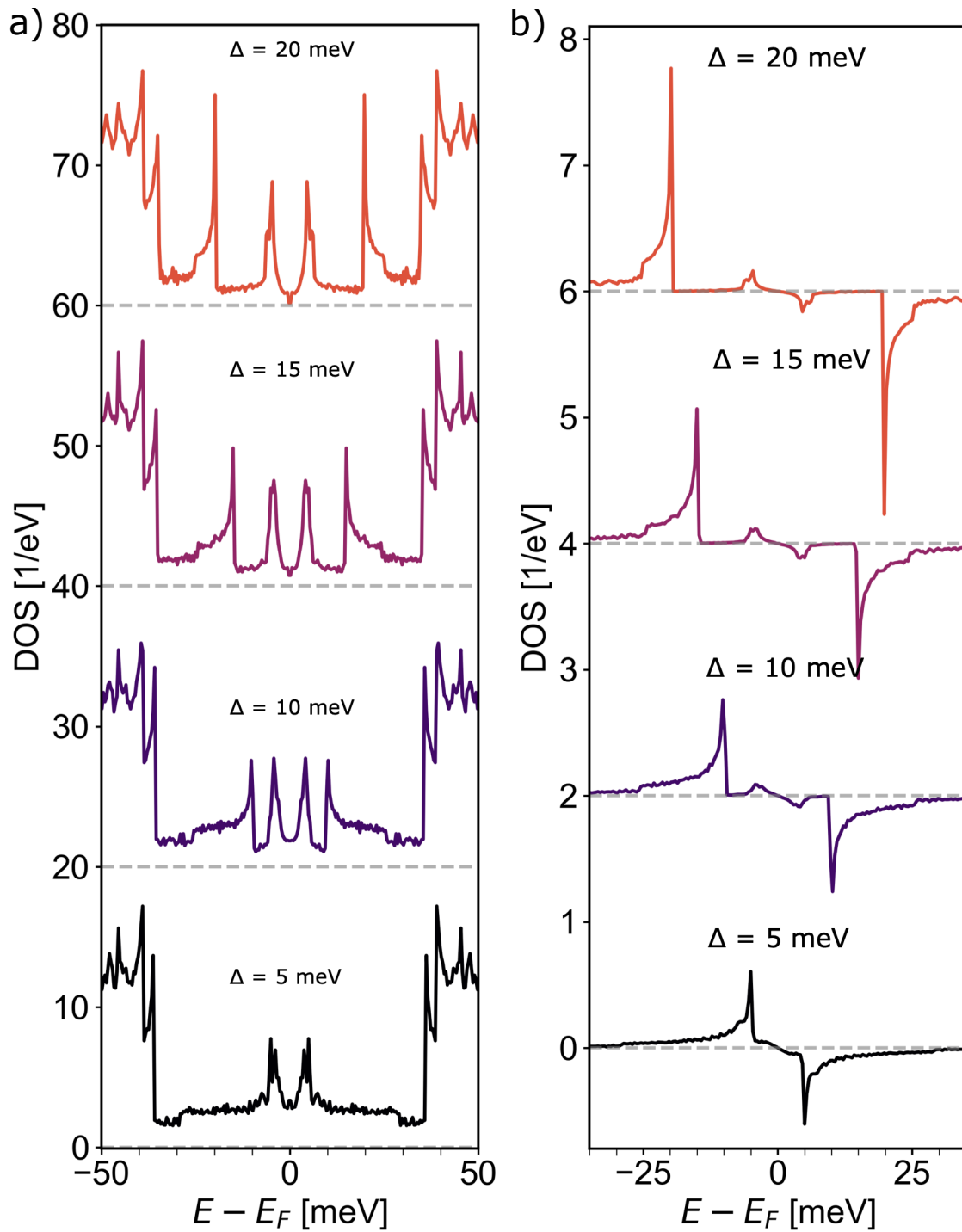
Figure 11: (a) SC–DOS and (b) anomalous DOS (right) for FeSe/STO varying Δ from 0 meV to 24 meV. The superconducting pairing potential is initialized only on the Fe atoms and the oxygen atoms of the TiO_2 terminated surface.
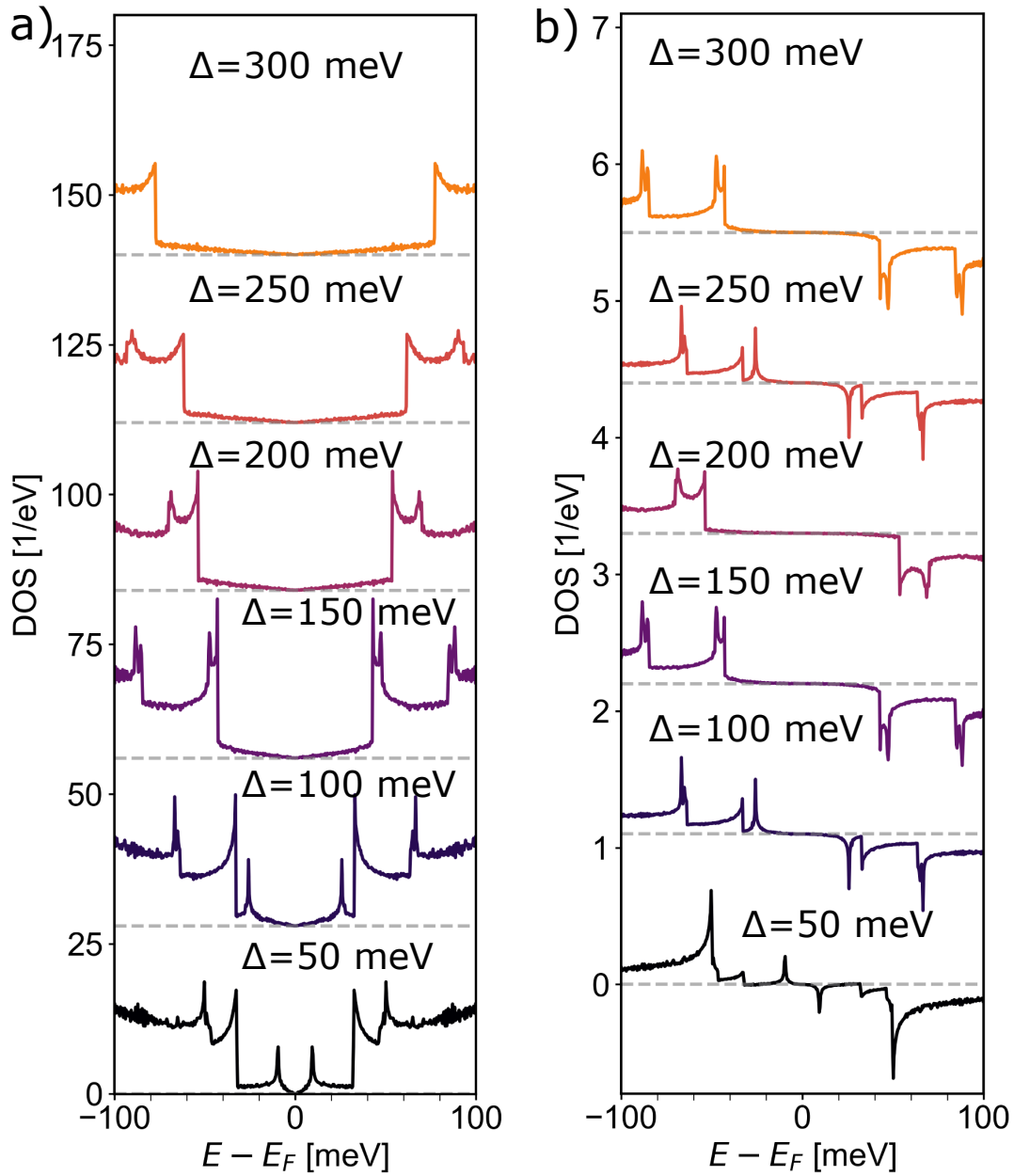
Figure 12: (a) SC–DOS and (b) anomalous DOS (right) for FeSe/STO varying Δ from 0 meV to 24 meV. The superconducting pairing potential is initialized only on the Fe atoms and the oxygen atoms of the TiO$_2$ terminated surface.
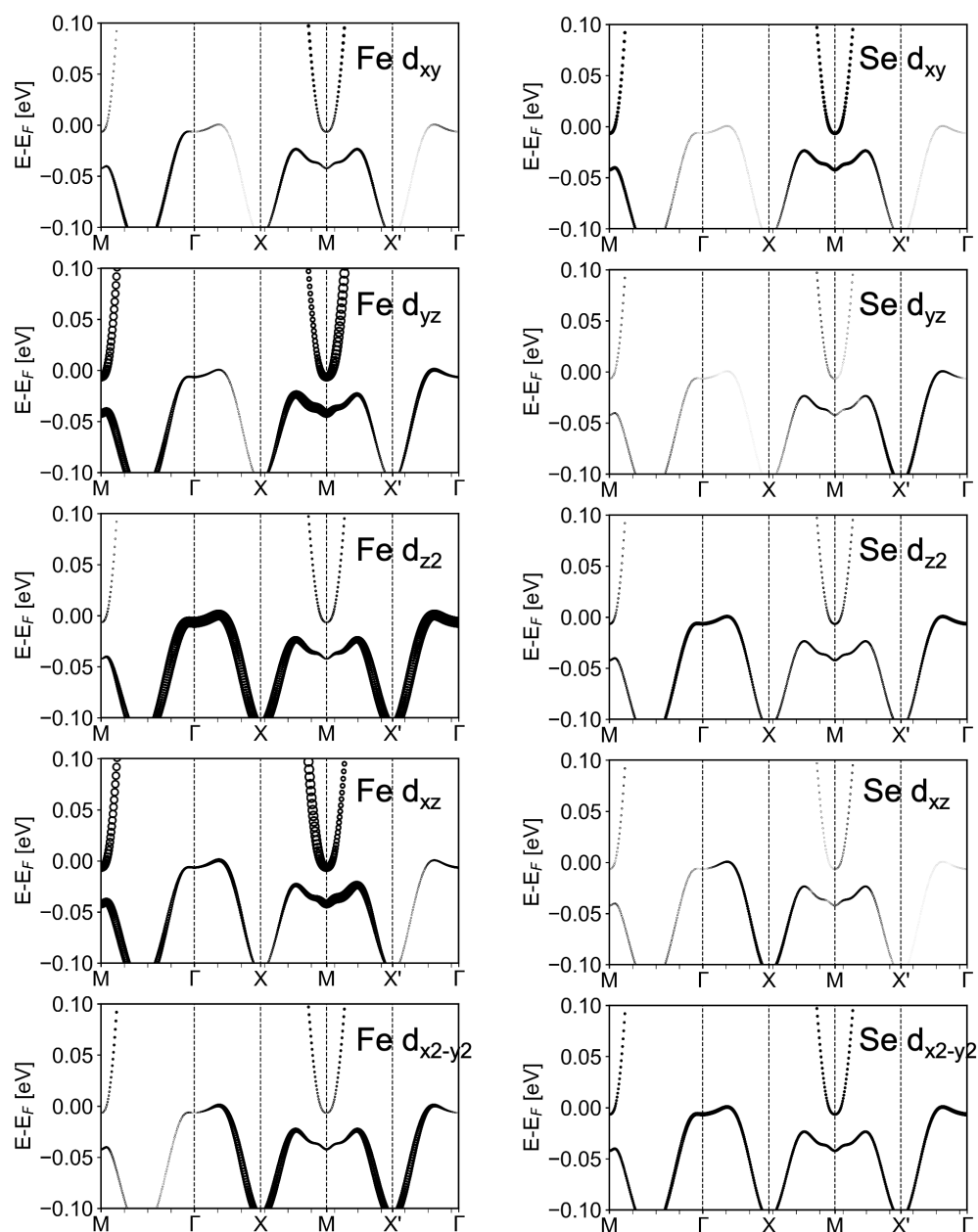
Figure 13: Electronic band structure of ML FeSe, projected on Fe(left) or Se(right) *d* orbitals.
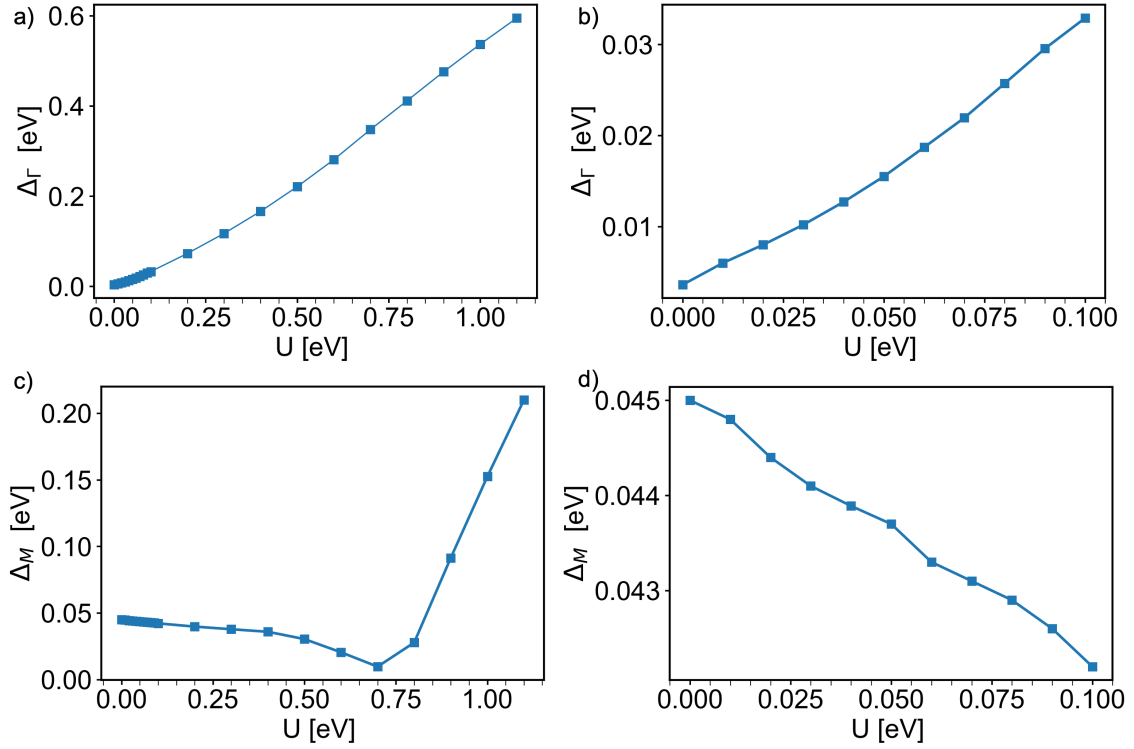
Figure 14: Convergence of the Hubbard U parameter towards ARPES results: (a) Energy difference between E_F and the last occupied state at Γ, Δ_Γ (b zoom-in) and (c,d) M, Δ_M, as a function of the Hubbard U term.
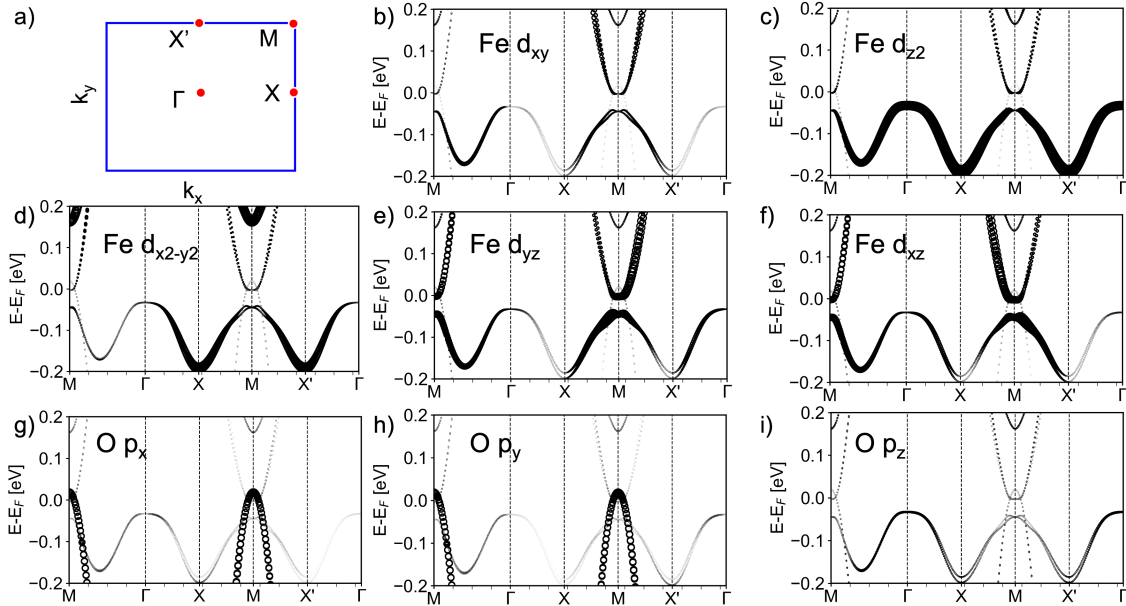
Figure 15: FeSe/STO: Schematic representation of the Brillouin Zone and its high-symmetry points. (a) Normal state electronic band structure projected on (b–f) d orbitals of Fe and (g–i) p–orbitals of O .
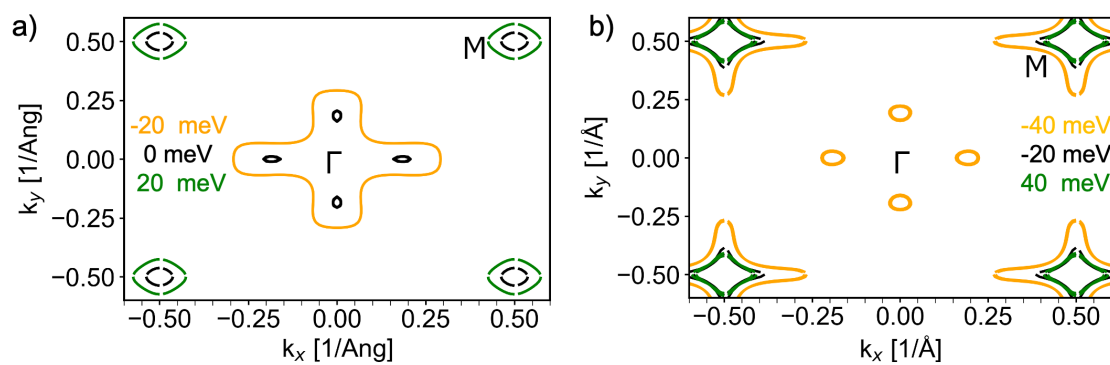
Figure 16: Fermi surfaces of (a) FeSe ML and (b) FeSe/STO in the normal state. The surfaces are shown as constant-energy cuts in the (E, k_x, k_y) frame. Energy values and corresponding colors are indicated in the legend.